

Giant Energy Harvesting via Maxwell Displacement Current Enhancement Using Metal Sheet Interspaced Hetero-Layer Structured Piezo-Composite Nanofiber Device

Biswajit Mahanty, Sujoy Kumar Ghosh, Gajula Prasad, Arunkumar Shanmugasundaram, and Dong-Weon Lee*

The limited performance of piezoelectric nanogenerators (PENGs) has hindered their practical applications in self-powered electronics. To address these limitations, this study presents a new design of a PENG that incorporates hetero-layer structured piezo-composite nanofibers with interspaced metal sheets. The hetero-layer structure consists of alternating layers of ferroelectric barium titanate (BT) nanoparticles interfaced with poly(vinylidene fluoride-co-trifluoroethylene) (P(VDF-TrFE)) composite nanofibers (P(VDF-TrFE)/BT), and conductive graphite nano-sheets (GNS)-embedded P(VDF-TrFE) composite nanofibers (P(VDF-TrFE)/GNS) mats. The inclusion of interspaced metal sheets in the device configuration enhances the stress concentration effect, thereby effectively distributing the applied mechanical vibrations. Simultaneously, the P(VDF-TrFE)/BT composite nanofibers improve the piezoelectric coefficient (187.86 pC N^{-1}), while the P(VDF-TrFE)/GNS composite nanofibers reduce the internal impedance of the device. These combined enhancements result in an increased Maxwell displacement current and power output. Consequently, the hetero-layer structured PENG exhibits an impressive open circuit voltage (V_{oc}) output of 350 V, a short circuit current (I_{sc}) output of 6 μA , and a power output of 3.62 W m^{-2} . Moreover, the developed PENG demonstrates extraordinary energy harvesting performance under harsh vibrations caused by human musculoskeletal movements, as well as subtle vibrations from heart pulses, emotional changes, and speech recognition. Additionally, the PENG shows its potential use in wearable self-powered wireless e-health systems.

traditional power sources like batteries and allow them to be useful as supplementary power sources for low-power electronic devices, ranging from consumer electronics to healthcare,^[1] implantable devices,^[2] environmental monitoring,^[3] wearable sensor networks^[4] and beyond. Despite the high performance of triboelectric nanogenerators (TENGs),^[5,6] in recent years, piezoelectric nanogenerators (PENGs) continues its flag of success in satisfying the industrial requirements and gaining more interest toward commercialization.^[7] There are still challenges to overcome, such as enhancing the power output performance, efficiency, reducing cost, as well as integrating the technology seamlessly into existing products and systems. In order to overcome the performance difficulties there are several materials to be useful. However, in contrast to high-performing mechanically stiff piezo-ceramics,^[8] polymer-based piezoelectric materials, such as poly(vinylidene fluoride) (PVDF) and its copolymers P(VDF-TrFE), have gained enormous attention in wearable applications due to their exceptional mechanical flexibility, ease of fabrication, environment friendly, and biocompatibility.^[9–12] The presence of all-trans β -phase in P(VDF-TrFE) leads

to spontaneous polarization of dipoles, resulting in piezoelectric behavior. To date, various techniques have been proposed to enhance the electroactive β -phase content including but not limited to mechanical stretching,^[13] electrical poling,^[14]

1. Introduction

By harnessing energy from the environmental and biomechanical vibrations, nanogenerators can eliminate the need for

B. Mahanty, G. Prasad, A. Shanmugasundaram, D.-W. Lee
MEMS and Nanotechnology Laboratory
School of Mechanical Engineering
Chonnam National University
Gwangju 61186, South Korea
E-mail: mems@jnu.ac.kr

S. K. Ghosh
Department of Condensed Matter Physics and Material Sciences
S.N. Bose National Centre for Basic Sciences
6, Block JD, Sector III, Salt Lake, Kolkata 700010, India
A. Shanmugasundaram, D.-W. Lee
Advanced Medical Device Research Center for Cardiovascular Disease
Chonnam National University
77 Yongbong-ro, Buk-gu, Gwangju 61186, Republic of Korea
D.-W. Lee
Center for Next-Generation Sensor Research and Development
Chonnam National University
Gwangju 61186, Republic of Korea

The ORCID identification number(s) for the author(s) of this article can be found under <https://doi.org/10.1002/adfm.202307723>

DOI: 10.1002/adfm.202307723

solution casting,^[15] filler incorporation,^[16] spin coating,^[17] and electrospinning.^[18] Among them, the in situ electrical poling process during electrospinning and the enhancement of the β -phase through the incorporation of high piezoelectric coefficient materials, such as barium titanate (BT),^[19] or conductive carbon-based fillers, such as graphite nano-sheet (GNS)^[20] into P(VDF-TrFE) matrix have been shown to significantly improve the piezoelectric performance of PENGs. In order to further improve the device performances, layer-by-layer structures of electrospun fiber mats were studied. For example, three-layered PEDOT-coated PVDF/PVDF/PEDOT-coated PVDF nanofibers-based PENG ($V_{oc} \sim 48$ V, $I_{sc} \sim 6$ μ A),^[21] six layers of alternatively placed polyurethane/BT and P(VDF-TrFE) nanofiber-based 3-D micropatterned stretchable substrate based PENGs ($V_{oc} \sim 9.3$ V, $I_{sc} \sim 189$ nA),^[22] oriented 12 layers PZT/PVDF electrospun nanofiber mat followed by hot pressing based PENGs ($V_{oc} \sim 83$ V, $I_{sc} \sim 7.6$ μ A),^[23] 5 layers unit of P(VDF-TrFE)/BT nanofiber based PENG ($V_{oc} \sim 84$ V, $I_{sc} \sim 1.32$ μ A).^[19] Still, the reported output power from the nanofiber-based PENGs to date was only in the range of a few microwatts due to the limited improvement of piezoelectric co-efficient in the range of 3.9–44 pC N⁻¹ (Table S1, Supporting Information). In addition, to date, layer-by-layer structured PENGs using electrospun nanofibers were usually fabricated with only the stacking of similar/homo layer piezoelectric materials, and very limited efforts were observed with the hetero layer structures. In fact, the performance of this homo-layers assembled PENGs is often limited by various factors, including high internal impedance,^[24] interfacial effects,^[25,26] polarization diminishing effect,^[27,28] non-uniform stress and electric field distribution,^[29] which can affect significantly on the overall output performances.^[19,21–23] To address these challenges and maximize the output performances in layer-by-layer PENGs, careful consideration on the layer configurations, selection of appropriate materials, and judicious device design are necessary. These parameters cumulatively enhance the Maxwell displacement current that is the main driving force for enhancement of the energy harvesting ability of a nanogenerator.^[30] The contribution of displacement current to TENG was extensively studied.^[31,32] To the best of our knowledge, till date, this concept is not initiated in the case of piezoelectric devices.

In this study, we present systematic Maxwell displacement current enhancement by modulating both device configuration and materials functionality. A hetero-structured PENG (HT-PENG) device was fabricated with interspace metal sheets by alternate stacking of BT NPs mixed P(VDF-TrFE) and graphite nano-sheets (GNS)-embedded P(VDF-TrFE) composite nanofibers mats as piezoelectric active layers. The optimized six-layered HT-PENG generated a voltage output of 350 V, current output of 6 μ A and power output of 3.62 W m⁻². While BT NPs effectively improved the piezoelectric co-efficient through interfacial interactions with the P(VDF-TrFE) chains, on the other hand, GNS mainly facilitated the charge transport by lowering the internal impedance along with the improvement of the β -phase. Additionally, the interspaced electrodes impose the stress concentration effect by uniformly distributing the external vibrations to each layer of piezo-nanofibers. Owing to its excellent sensitivity, the hetero-structured PENG has been effectively utilized as a portable power source, biomechanical energy harvester,

physiological signal monitoring, and wireless signal transferring sensor.

2. Results and Discussion

2.1. Device Configuration to Improve Maxwell Displacement Current

A schematic of the designed piezoelectric device is depicted in Figure 1a. The device was composed of hetero-layer structure of P(VDF-TrFE) composite nanofibers with interspaced metal sheets. The hetero-layer structure was comprised of alternatively placed P(VDF-TrFE)/GNS and P(VDF-TrFE)/BT composite nanofiber mats. The cross-sectional SEM image of the hetero-layer P(VDF-TrFE) composite nanofibers-based piezoelectric device is shown in Figure 1b. In generally, piezoelectric devices composed of multi-stacking layer structures generated higher electrical energy compared to that of the single-layer piezo-device.^[33] This is due to the polarization (P_s) sum up from each piezo-layer device cumulatively enhancing volume charge density ($\rho_b = -\nabla \cdot P_s$), surface charge density ($\sigma_b = P_s \cdot n$) and subsequently Maxwell's displacement current. According to the basic mechanism of nanogenerator, Maxwell displacement current ($J_D = \frac{\partial D}{\partial t} + \frac{\partial P_s}{\partial t} = \epsilon \frac{\partial E}{\partial t} + \frac{\partial P_s}{\partial t}$) due to the bound charges is the main driving force for generating an internal electric field and current output ($I_D = \int J_D \cdot ds$) from piezoelectric device under mechanical impact that induces capacitive conduction current collected through an external circuit.^[34] Therefore, Maxwell displacement current enhancement is one of the main strategies for improvement of the energy harvesting ability of nanogenerator. Considering the displacement current equation of a polarized media (due to bound charges) as, $J_D = (e)_{ijk} (\frac{\partial S}{\partial t})_{jk}$ (where, $(e)_{ijk}$ is the piezoelectric coefficient and $(\frac{\partial S}{\partial t})_{jk}$ is the applied strain rate induced by applied force), there are two ways to enhance the Maxwell displacement current. One is to improve the stress confinement/concentration effect that can improve $(\frac{\partial S}{\partial t})_{jk}$ and another way is to improve the piezoelectric coefficient $(e)_{ijk}$. In this work, we have improved both factors. Theoretical calculation shows that, instead of mere stacking of electrospun nanofibers, when we placed interspace metal sheet in between the stacked nanofiber mats, stress was concentrated on the interspaced metal sheets (Figure 1c). As a result of this stress concentration effect, each layer of the stacked piezo-nanofiber mat experienced almost a similar amount of applied stress (Figure 1d). In case of the piezoelectric device/nanogenerator (PENG) without inter-layer metal sheet, applied stress was highest only to the top piezo-layer while lower piezo-layers experienced less amount of stress as the applied stress was attenuated during passing through the dielectric media (Figure 1c,d). Therefore, $(\frac{\partial S}{\partial t})_{jk}$ was higher for stacked piezo-nanofiber mat with inter-space metal sheets compared to that of without metal sheets. As a result, the piezoelectric device with interspacing metal sheet generated higher Maxwell displacement field (D , surface average ~ 64 nC m⁻²) compared to that of the device without interspace metal sheet (D , surface average ~ 56 nC m⁻²) (Figure 1e). This displacement field generated by displacement current is the main driving force for power generation of the piezoelectric device under iterative mechanical

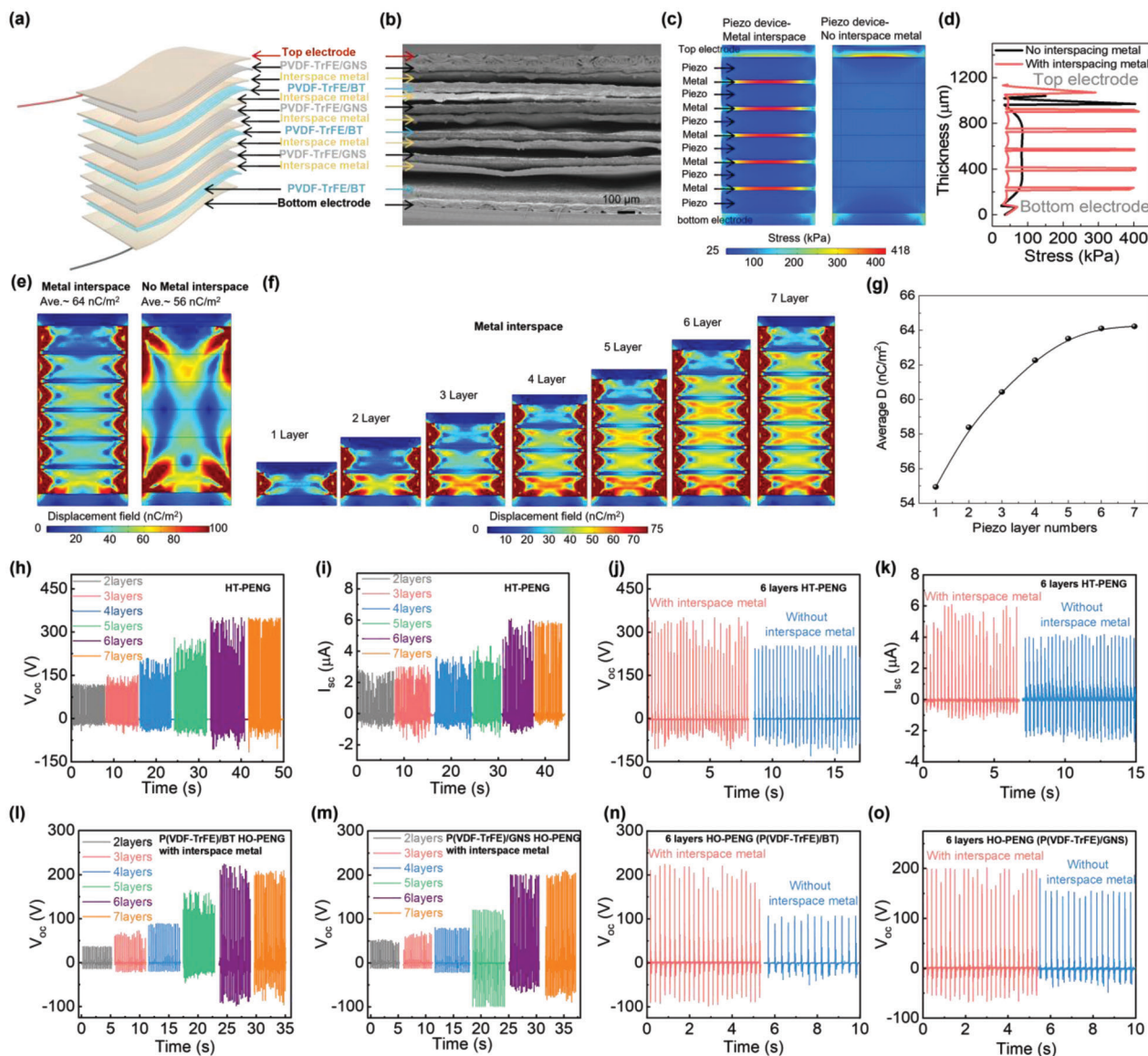


Figure 1. The concept of hetero-layer structure PENG (HT-PENG). a) The schematic of layer-by-layer hetero-structure PENG with interspace metal sheet. b) Cross-sectional SEM image of the HT-PENG. c) Theoretical simulation result of applied stress distribution profile image and d) thickness-dependent corresponding graph. e) Theoretical simulation of Maxwell displacement field distribution for six-layer device with and without interspace metal sheet and with increasing layer numbers with interspace metal sheet. The energy harvesting performances of the HT-PENG with several stacking layers in terms of (h) open circuit voltage (V_{oc}) and (i) short-circuit current (I_{sc}) of the HT-PENGs. j) The V_{oc} and k) I_{sc} of the optimized 6 layers HT-PENG. l) The V_{oc} of the P(VDF-TrFE)/BT and m) the P(VDF-TrFE)/GNS based HO-PENG with different stacked layers. n) The V_{oc} of the six layers P(VDF-TrFE)/BT and o) P(VDF-TrFE)/GNS based HO-PENG.

impact. Theoretical calculation further indicated that D values increase up to the six layers of piezo-nanofibers and almost saturated for the seventh piezo-layer (Figure 1f,g; Figure S1 and Associate Discussion S1, Supporting Information). Experimentally, we have prepared the hetero-layer P(VDF-TrFE) composite nanofibers based PENG (HT-PENG) as shown in Figure 1a with interspaced metal sheet and observed the increasing trend of open-circuit voltage (V_{oc}) and short circuit current (I_{sc}) with increasing numbers of piezo-layers and six layers comprising HT-PENG generated maximum $V_{oc} \approx 350$ V (Figure 1h) and $I_{sc} \approx 6$ μ A (Figure 1i) under the iterative compressive stress of 93.7 kPa.

In addition, we have also prepared six layers based HT-PENG without interspaced metal sheet where we have observed lower $V_{oc} \approx 250$ V (Figure 1j) and $I_{sc} \approx 4$ μ A (Figure 1k) compared to that of with interspaced metal sheet. These results further strengthen the importance of interspaced metal sheet for improving the Maxwell displacement current and consequently device performance. From materials perspective, piezoelectric coefficient improvement is another factor for improving the Maxwell displacement current. In order to improve the piezoelectric coefficient, we have prepared BT nanoparticles incorporated P(VDF-TrFE) composite nanofiber and GNS-embedded P(VDF-TrFE)

composite nanofibers. The enhanced piezoelectric properties of the composite nanofiber were evaluated in terms of generated voltage and current output under compressive pressure of 93.7 kPa and discussed later. The important factor is that the mere stacking of similar/homo-layer structured PENG (HO-PENG) composed of only P(VDF-TrFE)/BT or P(VDF-TrFE)/GNS composites nanofiber mats with interspaced metal sheet did not guarantee an erroneous enhancement of voltage and current output. While the six layers of P(VDF-TrFE)/BT composites nanofiber-based HO-PENG with interspaced metal sheet generated maximum $V_{oc} \approx 220$ V (Figure 1l) and $I_{sc} \approx 1.6$ μ A (Figure S2a, Supporting Information) on the other hand six layers of P(VDF-TrFE)/GNS composites nanofiber based HO-PENG with interspaced metal sheet generated $V_{oc} \approx 200$ V (Figure 1m) and $I_{sc} \approx 3$ μ A (Figure S2b, Supporting Information) that are lower than that of the hetero-layer structures of six-layered P(VDF-TrFE)/BT–P(VDF-TrFE)/GNS composites nanofiber mats with interspaced metal sheet ($V_{oc} \approx 350$ V, $I_{sc} \approx 6$ μ A in Figure 1h,i). In fact, six-layered P(VDF-TrFE)/BT and six-layered P(VDF-TrFE)/GNS-based HO-PENG with interspaced metal sheet generated higher $V_{oc} \approx 220$ V and $V_{oc} \approx 200$ V respectively compared to that of without metal sheet ($V_{oc} \approx 100$ V (Figure 1n) and $V_{oc} \approx 150$ V (Figure 1o) respectively). It is important to note that owing to the ferroelectric property of BT nanoparticles, P(VDF-TrFE)/BT composites nanofiber possessing higher piezoelectric co-efficient (evidenced later) shown higher voltage output ($V_{oc} \approx 220$ V) compared to P(VDF-TrFE)/GNS composites nanofiber ($V_{oc} \approx 200$ V) based HO-PENG, while due to the conducting nature of graphite nanosheet, the P(VDF-TrFE)/GNS composites nanofiber possessing higher conductivity (Figure S3, Supporting Information), lowers the internal impedance of HO-PENG (evidenced later) and shown higher current output ($I_{sc} \approx 3$ μ A) compared to P(VDF-TrFE)/BT composites nanofiber ($I_{sc} \approx 1.6$ μ A) (Figure S2a,b, Supporting Information). Therefore, when we prepared hetero-layer structured PENG using alternatively stacking of P(VDF-TrFE)/BT and P(VDF-TrFE)/GNS composites nanofiber mats, the resultant PENG generated both higher $V_{oc} \approx 350$ V and $I_{sc} \approx 6$ μ A (Figure 1h,i). In order to get a clear idea about the role of BT nanoparticles and GNS in enhancing voltage output and current output respectively, the following explanation is provided. The voltage output from a piezoelectric device depends on the internal electric field generation ($V = \int_0^x \vec{E} \cdot d\vec{x}$) and current output depends on the Maxwell's displacement current ($I_D = \int J_D \cdot ds$) driven by bound charges. The addition of BaTiO₃ nanoparticle into the P(VDF-TrFE) enhanced the local electric field of polymer matrix at the surface interface of nanoparticles considering Gauss's law (suppose, we consider the interface between P(VDF-TrFE) (permittivity: $\epsilon_{P(VDF-TrFE)}$) and BT (permittivity: ϵ_{BT})) and closed Gaussian surface at the interface divided into two parts, one with polymer and another with BT and uniform electric field E_0 (during electrospinning) crosses the interface. Applying Gauss's law separately to each part of the surface revealed, total electric flux through the closed surfaces were, $\Phi_{E_{P(VDF-TrFE)}} = \frac{1}{\epsilon_{P(VDF-TrFE)}} \iiint \rho_{P(VDF-TrFE)} dV_{P(VDF-TrFE)}$, and $\Phi_{E_{BT}} = \frac{1}{\epsilon_{BT}} \iiint \rho_{BT} dV_{BT}$ and considering $\rho_{P(VDF-TrFE)}$ and ρ_{BT} same, the electric field will be higher in P(VDF-TrFE) region compared to BT. Note that, at the interface region, $\rho_{P(VDF-TrFE)} > \rho_{BT}$ due to induced inter-

facial polarization charges through interaction between P(VDF-TrFE) chain and BT nanoparticles).^[35] As a result, macromolecular P(VDF-TrFE) chain at the BT nanoparticle interface experience higher electric field compared to other region during electrospinning and P(VDF-TrFE)/BT nanofiber composite possess higher polar β -phase and crystallinity due to better chain alignment compared to pure P(VDF-TrFE) and P(VDF-TrFE)/GNS nanofiber. These effects cumulatively enhanced the overall polarization keeping impedance high that results higher voltage output by enhancing the internal electric field.

On the other hand, owing to the higher charge carrier mobility of graphite nano-sheets (GNS), they provide an electric flux path^[36] or conducting network path^[37] between the polymer chains through the interfacial interaction during electrospinning that reduced the overall impedance of the composite nanofiber and makes it easier to electrically pole the polymer chains^[38] enhancing resultant displacement polarization. Both higher surface and bulk conductivities of the P(VDF-TrFE)/GNS (due to the conducting nature of GNS^[37]), higher contribution from both of the effective surface and volume charge densities cumulatively enhanced the current output compared to P(VDF-TrFE) and P(VDF-TrFE)/BT nanofibers where only surface-bound charge density (σ_b) contributes to the current output due to higher impedance. Note that, due to the conducting nature, graphite nano-sheets possess free charge carrier (σ_f and ρ_f).^[39] Considering the principle of superposition in electrostatics, the effective surface charge density (σ_{eff}) is the combination of surface-bound charge density (σ_b) from P(VDF-TrFE) and surface free charges (σ_f) from GNS, where σ_b and σ_f does not interact to each other as the GNS form discrete conducting path in P(VDF-TrFE) matrix (below percolation threshold).^[40] Similarly, effective volume charge density (ρ_{eff}), can be written as, $\rho_{eff} = \rho_b + \rho_f$. As a result, we obtained higher current output from the P(VDF-TrFE)/GNS compared to pure P(VDF-TrFE) and P(VDF-TrFE)/BT composites. The enhancement of current output from the nanogenerators due to the conducting fillers was also observed previously reported works.^[41–43] In summary, both the integrated voltage (resulting from the integration of the electric field generated by interfacial polarization caused by BT filler) and the differentiated current (the time derivative of the electric field within the poled paths of conducting filler below the percolation threshold) exhibit time-varying characteristics, but they emphasize different aspects of the material's response, and their nature of response is indeed distinct. The integrated voltage, although subject to temporal variations, primarily represents the steady-state response resulting from the cumulative effects of polarization in the insulating BT nanoparticles. On the other hand, the differentiated current focuses on the dynamic response associated with the conducting graphite nanosheets and their capacity to transport charges in response to changes in the electric field.

2.2. Effect of BaTiO₃ Nanoparticles (BT NPs) and Graphite Nano-Sheet (GNS) to Improve the Nanofiber Crystallinity and β -Phase Content

It is important to note that β -phase content and degree of crystallinity are directly proportional to the dipolar orientation and hence, the piezoelectricity of the materials.^[44] The effect of

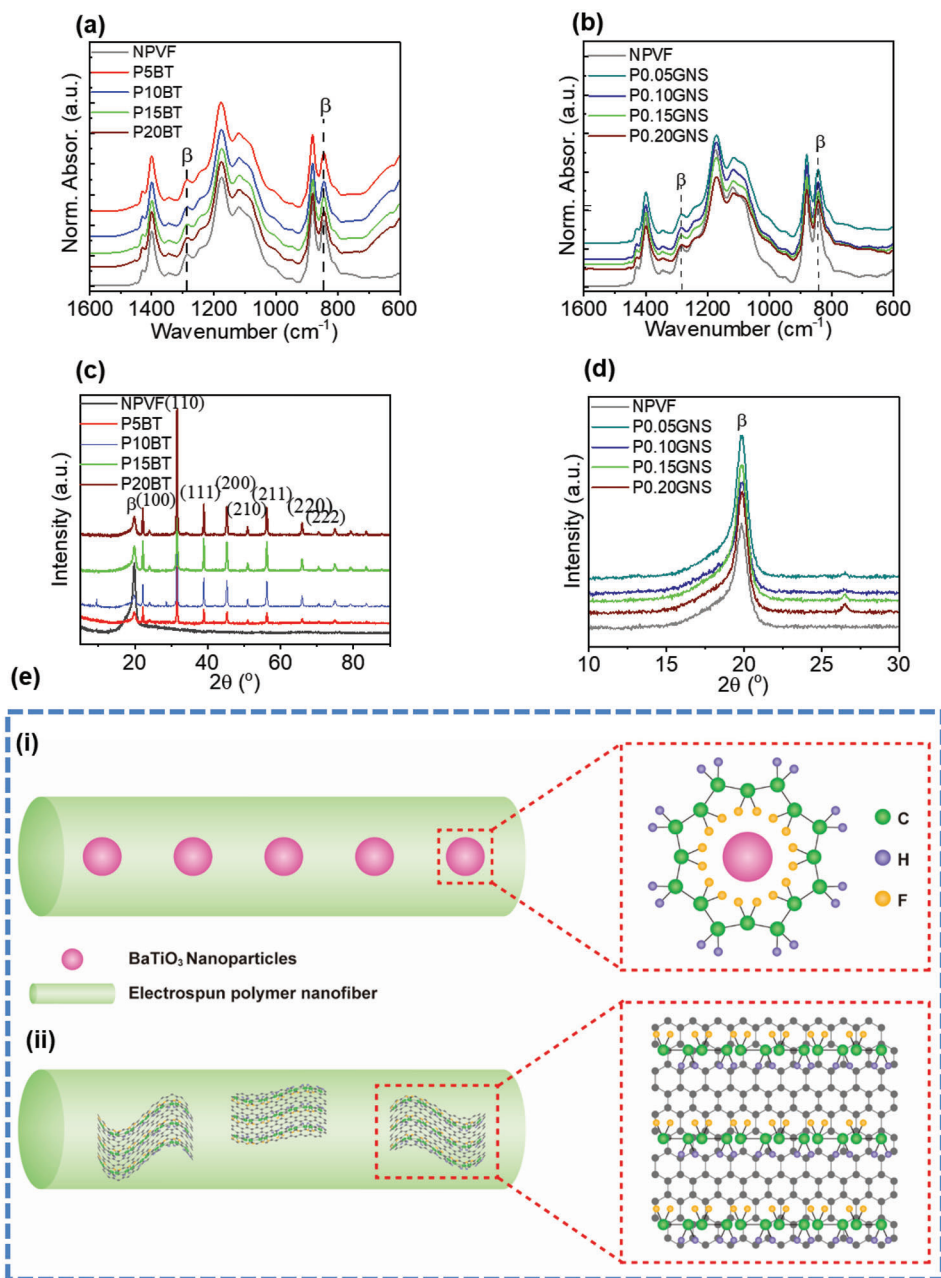


Figure 2. FT-IR spectra of a) NPVF and P(VDF-TrFE)/BT, b) NPVF and P(VDF-TrFE)/GNS composite nanofibers. The XRD pattern of c) NPVF and P(VDF-TrFE)/BT, d) NPVF and P(VDF-TrFE)/GNS composite nanofibers, e) The mechanism diagram of β phase formation on (i) BT nanoparticles in the P(VDF-TrFE)/BT composite nanofiber and (ii) graphite nanosheets in the P(VDF-TrFE)/GNS composite nanofiber.

incorporation of BT NPs (5–20 wt.%) and GNS (0.05–0.2 wt.%) into pure P(VDF-TrFE) nanofibers in the form of β -phase and crystallinity content were investigated through Fourier transform infrared (FT-IR) spectra and X-ray diffraction (XRD) analyses (**Figure 2a–d**). The FT-IR spectra (**Figure 2a,b**) revealed that the pure P(VDF-TrFE) nanofibers (NPVF) and the composite nanofibers showed vibrational bands at 841 and 1286 cm^{-1} , which were attributed to the piezoelectric β -crystalline phase.^[10] The formation of the piezoelectric β -crystalline phase in the pure P(VDF-TrFE) nanofibers could be attributed to the simultane-

ous poling and stretching during the electrospinning process.^[33] The FTIR analysis^[18] shows that among several concentration of BT nanoparticles, P(VDF-TrFE)/BT composite nanofiber with 10 wt.% BT nanoparticles (named as P10BT, details are provided in Experimental Section) shown the highest fraction of the β -phase ($\approx 93\%$) while among several concentrations of GNS, P(VDF-TrFE)/GNS composite nanofiber with 0.10 wt.% GNS (P0.10GNS) shown maximum fraction of β -phase content ($\approx 77\%$) that were higher than that of the pure P(VDF-TrFE) nanofibers ($\approx 75\%$). Furthermore, the dipolar orientation of the

CH_2/CF_2 dipoles (considering the absorption ratio of 881 and 845 cm^{-1} peaks in FTIR spectra)^[45] within P(VDF-TrFE)/BT composite nanofiber was highest with 10 wt.% BT nanoparticles while with 0.10 wt.% GNS the P(VDF-TrFE)/GNS composite nanofiber shown maximum orientation (Figure S4, Supporting Information).

The XRD analyses (Figure 2c) showed that the NPVF nanofibers and all the P(VDF-TrFE)/BT nanofibers exhibited a diffraction pattern at 19.9° , which corresponds to the sum of (110) and (200) reflections of the β -polar phase.^[46] The P(VDF-TrFE)/BT composite nanofibers showed additional diffraction peaks at $2\theta = 22.1, 29.4, 32.5, 45.4, 48.1, 56.0, 62.7$, and 69.2° , which correspond to the (100), (110), (111), (200), (210), (211), (220), and (222) crystallographic planes of the tetragonal phase of BT (JCPDS (# 073644) ICDD pattern), indicating that the BT NPs were successfully incorporated into the P(VDF-TrFE) nanofibers.^[47,48] The XRD patterns of the pure BT NPs is shown in Figure S5a (Supporting Information). The Raman spectroscopy confirms the tetragonal phase (Figure S5b, Supporting Information) of BT nanoparticle that shows strong ferroelectricity property (Figure S5c, Supporting Information). The P(VDF-TrFE)/GNS composite nanofibers exhibited a diffraction pattern at 19.9 and 26.3° , which were attributed to the β -crystalline phase and 002 planes arising from the graphitic carbon crystal structure (Figure 2d).^[49,50] The XRD patterns of the pure GNS is shown in Figure S5d (Supporting Information). This indicates that the GNS were successfully incorporated into the P(VDF-TrFE) nanofibers matrix.

The degree of crystallinity (χ_c) of the pure and nanocomposite nanofibers were estimated from the XRD pattern using the curve deconvolution process, (Figure S6, Supporting Information), and calculated using the equation, $\chi_c = \frac{\sum A_{cr}}{\sum A_{cr} + \sum A_{amr}} \times 100\%$, where $\sum A_{cr}$ and $\sum A_{amr}$ are the total integral area due to crystalline peaks and amorphous halo respectively.^[10] It has been observed that the highest degree of crystallinity (χ_c) in the P(VDF-TrFE)/BT and P(VDF-TrFE)/GNS composite nanofibers were ($\approx 66\%$) and ($\approx 55\%$) in 10 wt.% BT and 0.10 wt.% GNS, respectively, that were higher than that of NPVF nanofibers ($\approx 50\%$). The polymer chain alignment through interfacial interaction and consequently dipolar alignment^[18] is the main reason for enhancing the crystallinity of P(VDF-TrFE) based composite nanofibers. Owing to the ferroelectric nature and higher impedance, the effect of BT nanoparticle to improve the crystallinity of P(VDF-TrFE) nanofiber was higher than that of the GNS as discussed in Section 2.1. The comparison of crystallinity (χ_c) with filler concentration of BT and GNS in P(VDF-TrFE)/BT, P(VDF-TrFE)/GNS composite nanofibers respectively are presented in Figure S7 (Supporting Information). In overall, effect of BT nanoparticles to improve the β -phase content and degree of crystallinity (χ_c) was more pronounced compared to that of the GNS in composite nanofibers. This improvement is primarily from interfacial interaction with BT nanoparticle (Figure 2e-i) and GNS surfaces (Figure 2e-ii) with $-\text{CH}_2/-\text{CF}_2$ groups of P(VDF-TrFE) chain. In the case of BT nanoparticles, during electrospinning, the ferroelectric domains of BT nanoparticles are aligned under the presence of electric field. This spontaneous polarization enhanced the average local electric field leading to enhanced polarizability at the interface of BT nanoparticles and P(VDF-TrFE) chain, which

increased the piezoelectricity and impeded the migration as well as accumulation of the space charge in nanocomposites.^[51] On the other hand, GNS interacted P(VDF-TrFE) nanocomposites enhanced the space charge conduction due to high charge carrier mobility of conducting GNS leading to more electron flow within PENG. Experimentally, we have observed that P(VDF-TrFE)/GNS composite nanofiber possesses higher conductivity than that of P(VDF-TrFE)/BT composite nanofiber (Figure S3 and Table S2, Supporting Information). In case of P(VDF-TrFE)/GNS composite nanofibers, the H atoms of $-\text{CH}_2/-\text{CF}_2$ dipoles in P(VDF-TrFE) chains tend to approach the GNS surface (Figure 2e-ii). This proximity is induced by the electrostatic interaction between the sp^2 hybridized high-electronegativity C atoms with π orbitals in GNS and the low electronegativity H atoms in P(VDF-TrFE) chains.^[52] As a result of this interaction, the $-\text{CF}_2-$ moieties in the composite nanofibers are projected away from the GNS surface, promoting the formation of the β -crystalline phase. This organized arrangement of dipoles contributes to a higher net polarization in the crystalline lattice, resulting in improved piezoelectric properties.

The surface morphology of the nanofibers was observed via field emission scanning electron microscopy (FE-SEM) images. The pure P(VDF-TrFE) nanofibers (NPVF) were prepared without any bead defects and of uniform diameter ($\approx 634 \pm 153\text{ nm}$) (Figure 3a; Table S3, Supporting Information). On incorporation of 10 wt.% BT nanoparticles (Figure 3b) and 0.10 wt.% GNS (Figure 3c) into the P(VDF-TrFE), the surfaces of the nanofibers were rougher and the diameter decreased to $400 \pm 259\text{ nm}$ and $588 \pm 460\text{ nm}$ respectively (Table S3, Supporting Information) due to the increased total charges originating from the interface of BT NPs and GNSs, subsequently enhancing the exerted force in the electrospinning jet and reducing fiber diameter.^[53] The surface morphology of the P(VDF-TrFE)/BT and P(VDF-TrFE)/GNS composite with several concentrations of BT nanoparticles and GNS are shown in Figures S8 and S9 (Supporting Information), respectively. In addition, the diameter of all of the nanofibers are evaluated and shown in Table S3 (Supporting Information). Energy dispersive X-ray spectroscopy (EDS) and corresponding elemental mapping further confirm the presence and uniform distribution of all elements in pure P(VDF-TrFE) (in particular, carbon (C) and fluorine (F) in Figure 3a), P(VDF-TrFE)/BT (10 wt.%) composites nanofibers (in particular oxygen (O), barium (Ba), and titanium (Ti) elements from BT nanoparticles in Figure 3b) and P(VDF-TrFE)/GNS (0.1 wt.%) composite nanofibers (in particular carbon (C) in the coagulation of nanofiber due to GNS in Figure 3c).

Further EDS mapping and weight percentage of the elements in the rest of the composite nanofibers including pure BT nanoparticles and GNS is shown in Figures S8–S10 and Table S4 (Supporting Information). An increasing trend in the wt.% of Ba, Ti, and O content was observed with an increase in BT concentration to 10 wt.% (Table S4, Supporting Information). Nonetheless, upon further increment of BaTiO_3 wt.% in the P(VDF-TrFE)/BT, no significant changes in the elemental composition were detected, which could be attributed to the sedimentation of some BT NPs within the electrospinning tube during the electrospinning procedure.

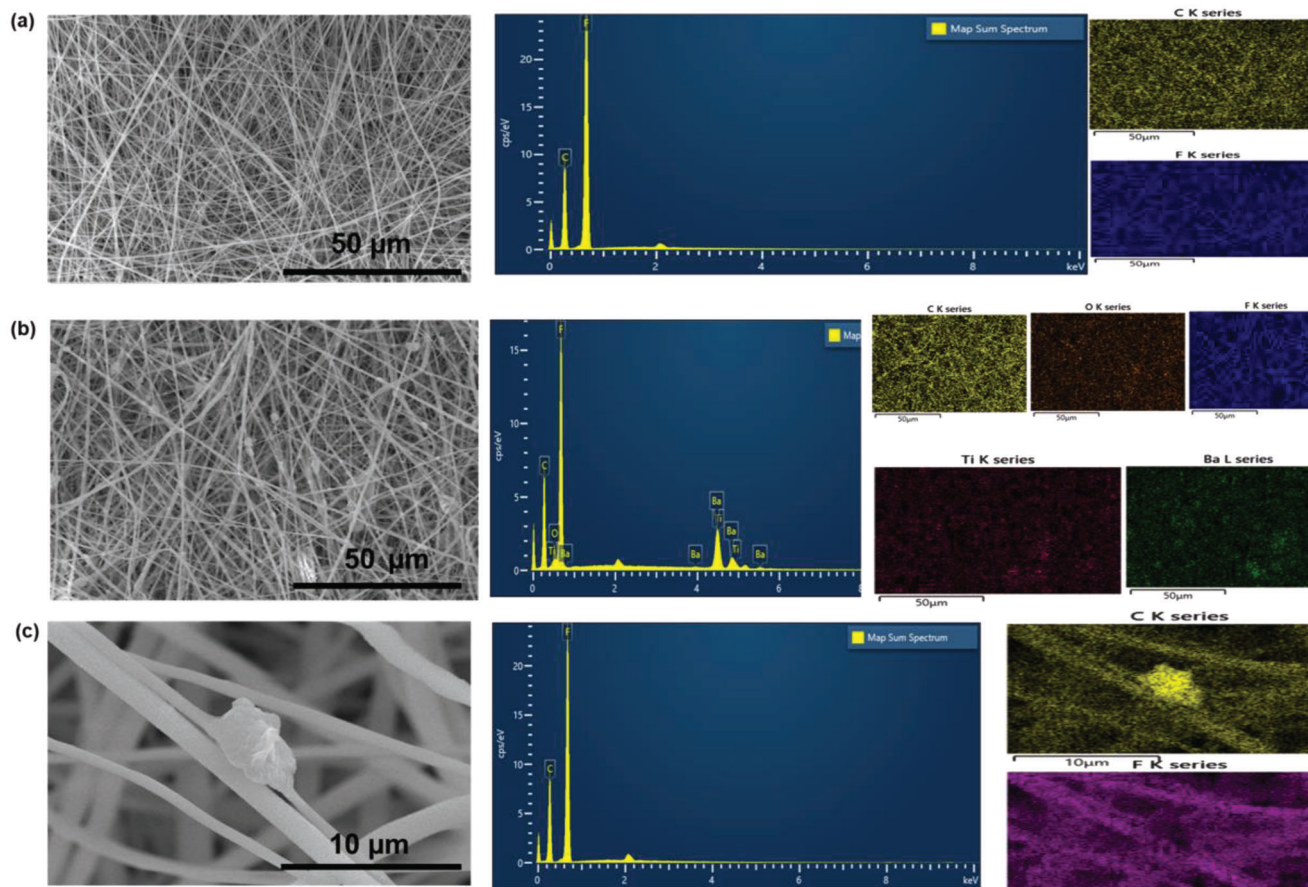


Figure 3. Field emission scanning electron microscopy (FE-SEM) images, energy dispersive X-ray spectroscopy (EDS), and elemental mapping of a) NPVF, b) P10BT, c) P0.10GNS nanofiber mats respectively.

2.3. Materials Functionality to Improve the Energy Harvesting Performance

In order to understand the materials functionality for improving the energy harvesting performance, several systematic studies were conducted by fabricating nanofibers-based single-layer piezoelectric nanogenerators (S-PENGs). The details of the fabrication process are provided in the Experimental Section. It has been observed that the pure P(VDF-TrFE) based S-PENG generated $V_{oc} \approx 4$ V and $I_{sc} \approx 0.25$ μA respectively under the iterative pressure of 93.7 kPa (Figure S11a,b, Supporting Information). On increasing concentration of BT NPs in the range of 5–20 wt.% (Figure 4a,b) the generated V_{oc} (Figure 4a) and I_{sc} (Figure 4b) were increased and reached a maximum value of 28 V and 1.6 μA respectively with the BT NPs concentration of 10 wt.% and beyond this concentration, the V_{oc} and I_{sc} were decreased. Similarly, V_{oc} (Figure 4c) and I_{sc} (Figure 4d) of the P(VDF-TrFE)/GNS (0.05 to 0.20 wt.%) composite nanofibers based S-PENG was also optimized where the maximum V_{oc} and I_{sc} of 22 V and 1.9 μA respectively is observed for GNS concentration of 0.10 wt.%, beyond which the V_{oc} and I_{sc} were decreased. The reduction in the V_{oc} and I_{sc} from the composite nanofibers was observed when dopant concentrations exceeded critical values (10 wt.% for BT NPs and 0.10 wt.% for GNS).

This phenomenon can be ascribed to the agglomeration of BT NPs and GNS within their respective nanofibers, which leads to diminished interfacial interactions and dopant sedimentation in electrospinning tubes, resulting in decreased β -phase content and degree of crystallinity.^[10] The optimized S-PENGs with P(VDF-TrFE)/BT and P(VDF-TrFE)/GNS exhibited a sevenfold and 5.5-fold enhancement in open circuit output voltage performance, respectively, compared to the pure P(VDF-TrFE) nanofibers. Henceforth, the two optimized S-PENGs based on 10 wt.% BT-based P(VDF-TrFE)/BT and 0.10 wt.% GNS-based P(VDF-TrFE)/GNS composite nanofibers were used for the fabrication of hetero-layer PENG. It is found that the magnitude in peak output voltage between compress and release conditions (i.e., positive and negative peaks) are detected to be different/asymmetric due to the difference in straining rate when applying and releasing the stress on the PENG.^[54,55] It is noteworthy that the arising positive output during finger touch is larger than the negative one during release motion due to fast pressing and slow releasing motions of human finger showing the dependence of the output voltage on the strain rate.^[56,57] In addition, the contribution of triboelectric potential is found to be negligible in comparison to that of the piezoelectric potential (Figure S12 and Associate Discussion S2, Supporting Information). Meanwhile, it is observed that P(VDF-TrFE)/BT

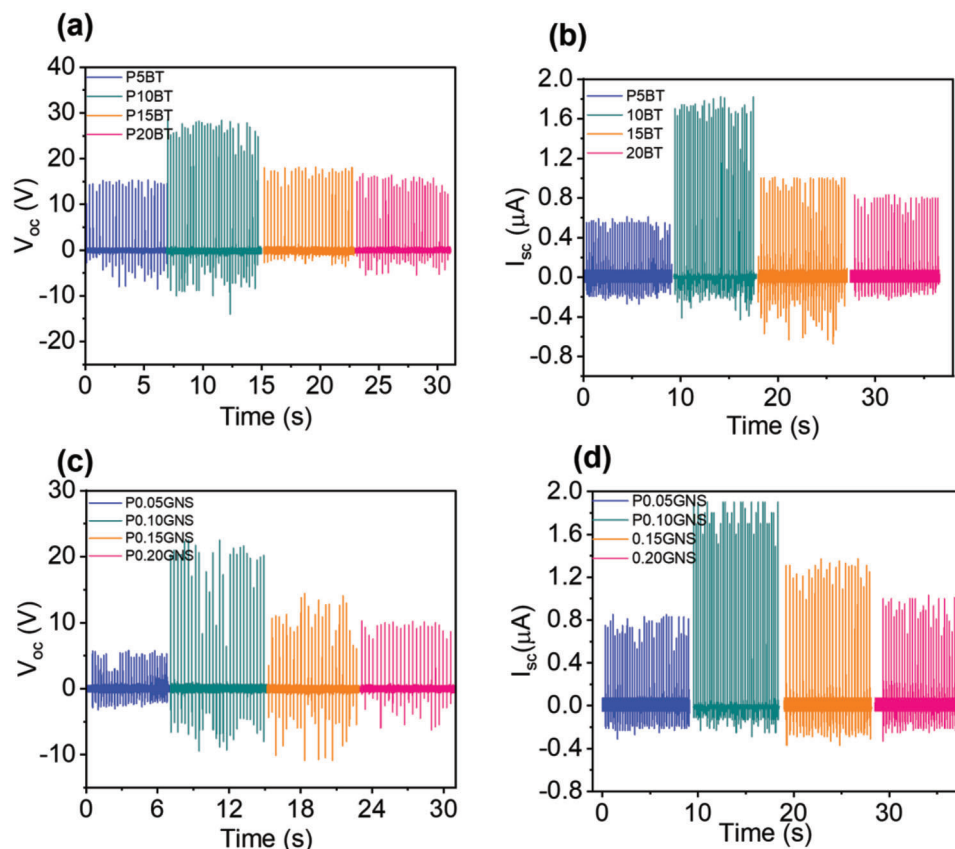


Figure 4. Piezoelectric performance of single-layered PENG (S-PENG). a) Open circuit output voltage and b) short circuit current for all P(VDF-TrFE)/BT composite nanofibers-based S-PENGs. c) Open circuit output voltage and d) short circuit current for all P(VDF-TrFE)/GNS composite nanofibers-based S-PENGs.

composite nanofibers based S-PENG generated higher open circuit output voltage compared to P(VDF-TrFE)/GNS nanofibers whereas P(VDF-TrFE)/GNS nanofibers generated higher short circuit current compared to that of the P(VDF-TrFE)/BT nanofiber. This phenomenon is attributed owing to the higher conductivity of the P(VDF-TrFE)/GNS nanofibers compared to P(VDF-TrFE)/BT nanofiber (Figure S3 and Table S2, Supporting Information). On the other hand, the reason for the higher voltage output is the ferroelectric property of the BT nanoparticles (Figure S5c, Supporting Information) for which P(VDF-TrFE)/BT nanofiber possess higher β -phase content, degree of crystallinity, and longitudinal piezoelectric coefficient (d_{33}) compared to P(VDF-TrFE)/GNS composite nanofibers. The d_{33} values of the nanofibers were calculated using quasi-static method, using the equation, $d_{33} = Q_e/F$ where, $Q_e = \int I_{sc} dt$ represents generated charge under the impact force (F) of 37.9 N.^[58] The highest piezoelectric coefficient (d_{33}) of ≈ 187.86 and ≈ 168 pC N⁻¹ for P(VDF-TrFE)/BT(10 wt.%) and P(VDF-TrFE)/GNS(0.10 wt.%) respectively is observed that were higher than previously developed P(VDF-TrFE) composite nanofibers (Table S1, Supporting Information). It is important to note that the pure P(VDF-TrFE) nanofiber possesses d_{33} of 36.46 that was consistent with the available literature.^[9] The estimated values of d_{33} for all other nanofibers are summarized in Table S5 (Supporting Information). We have also summarized the d_{33} values for all layers HT-

PENG and 6L HT-PENG without interface metal sheet in Table S6 (Supporting Information). In addition, the working mechanism of the S-PENGs is described in Figure S13 (Supporting Information) with Associate Discussion S3 (Supporting Information).

2.4. Sensitivity and Power Output Performance of Hetero-Layer Piezoelectric Nanogenerator

The sensitivity of the six layers HT-PENG was assessed by measuring the V_{oc} under low (1–2 kPa in Figure S14, Supporting Information) and medium (72.5–93.7 kPa in Figure 5a) pressure regions.

The linear proportionality of V_{oc} across pressures evaluated the pressure/mechano-sensitivity S_M of the HT-PENG was 20 ± 1.4 V kPa⁻¹ within 1–2 kPa regime and 13.45 ± 1.4 V kPa⁻¹ within 72.5–93.7 kPa pressure regions (Figure 5b). These values are closely related to the pressure ranges produced by human body movements, which are typically categorized as low-pressure (1–10 kPa) and medium-pressure (10–100 kPa) regimes.^[59] The mechano-sensitivity values of the HT-PENG are higher than those of recently reported TENGs and PENGs (Figure 5c).

The instantaneous voltage drop (V_L) (Figure 5d) and power density ($P = \frac{V_L^2}{AR_L}$, where A is the effective surface area)

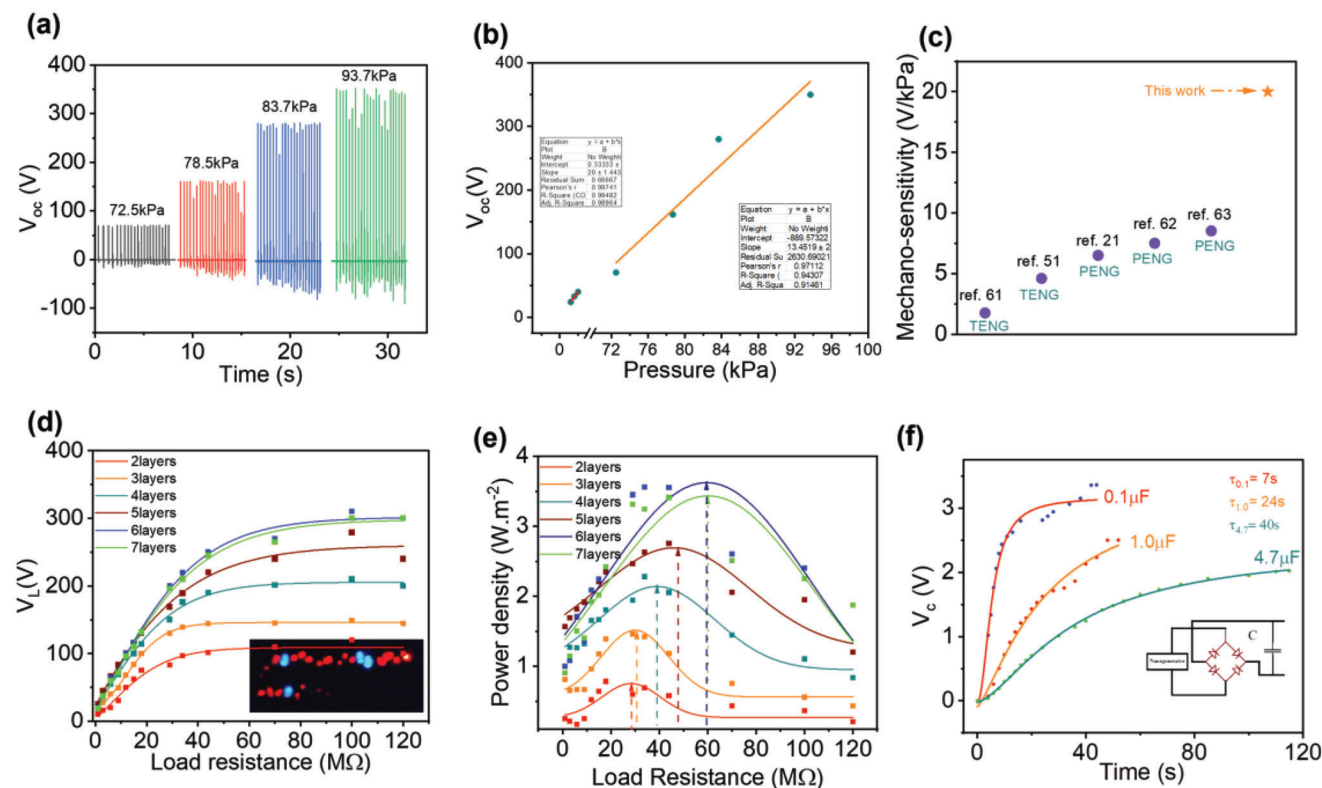


Figure 5. Sensitivity and output performance of HT-PENG. a) Pressure-dependent output open circuit voltage (V_{oc}) of the 6L HT-PENG, b) mechano-sensitivity plot of the 6L HT-PENG, c) mechano-sensitivity of reported piezoelectric based nanogenerators with the 6L HT-PENG, d) the variation in the output voltage with external load resistances of HT-PENG, e) the variation in the power density and external load resistances of HT-PENG, and f) capacitor charging behavior of the 6L HT-PENG at different capacitor values.

(Figure 5e) of the different (two-six) layers HT-PENG were measured under iterative applied pressure of 93.7 kPa while varying the external load resistance (R_L). The six-layer HT-PENG delivered the highest power density of 3.62 W m^{-2} at an R_L of $\approx 59.6 \text{ M}\Omega$, which means that internal impedance of the six-layer HT-PENG was $59.6 \text{ M}\Omega$. According to the circuit theory maximum power was delivered when impedance of the internal and external systems matched.^[60] The summary of the power density of all layers HT-PENG and corresponding load resistances are presented in Table S7 (Supporting Information). In the case of six layers P(VDF-TrFE)/BT-based HO-PENG the internal impedance ($68.7 \text{ M}\Omega$ at which power density was 1.42 W m^{-2} shown in Figure S15a, Supporting Information) was higher than that of the HT-PENG. On the other hand, the six layers P(VDF-TrFE)/GNS-based HO-PENG possesses lower impedance ($51.8 \text{ M}\Omega$ at which power density of 1.17 W m^{-2} shown in Figure S15b, Supporting Information) but due to lower voltage generation the power output was lower compared to HT-PENG. In fact, internal impedance of P(VDF-TrFE)/BT (10 wt.%) based single layer PENG was higher ($19 \text{ M}\Omega$ at which power density was 0.096 W m^{-2} shown in Figure S15c, Supporting Information) compared to that of P(VDF-TrFE)/GNS (0.1 wt.%) based single layer PENG ($18.4 \text{ M}\Omega$ at which power density was 0.062 W m^{-2} shown in Figure S15d, Supporting Information), respectively.

In addition, the generated power density of the HT-PENG is higher than that of the state-of-the-art nanofibers-based PENGs

(Table S1, Supporting Information). The superior instantaneous power density of the HT-PENG was sufficient to operate several commercial electronic units such as, an array of light-emitting diodes (LEDs) (image shown in right lower inset of Figure 5d; Video S1, Supporting Information), acoustic sensor module (Video S2, Supporting Information), and commercial capacitors with capacitances of 0.1, 1.0, and 4.7 μF (Figure 5f). The superiority of the capacitor charging performance was described in Associate Discussion S4 (Supporting Information) and compared in Table S8 (Supporting Information). To evaluate the long-term stability of the HT-PENG, cyclic fatigue testing was also conducted over several months where no degradation in the voltage output was observed that ensures the reliability in the energy harvesting performance (Figure S16, Supporting Information).

2.5. Self-Powered Wearable Sensor Applications

Owing to the superior sensitivity^[61–63] and power output, the six-layered HT-PENG was used to investigate the real-time human physiological signal monitoring by attaching the device to various body regions of interest (Figure 6a) and measuring the output signals from the device in terms of current (Figure 6b) and voltage (Figure S17, Supporting Information) output. For example, when the device was positioned on the throat, it exhibited a consistent sensing ability in response to thoracic pressure changes resulting

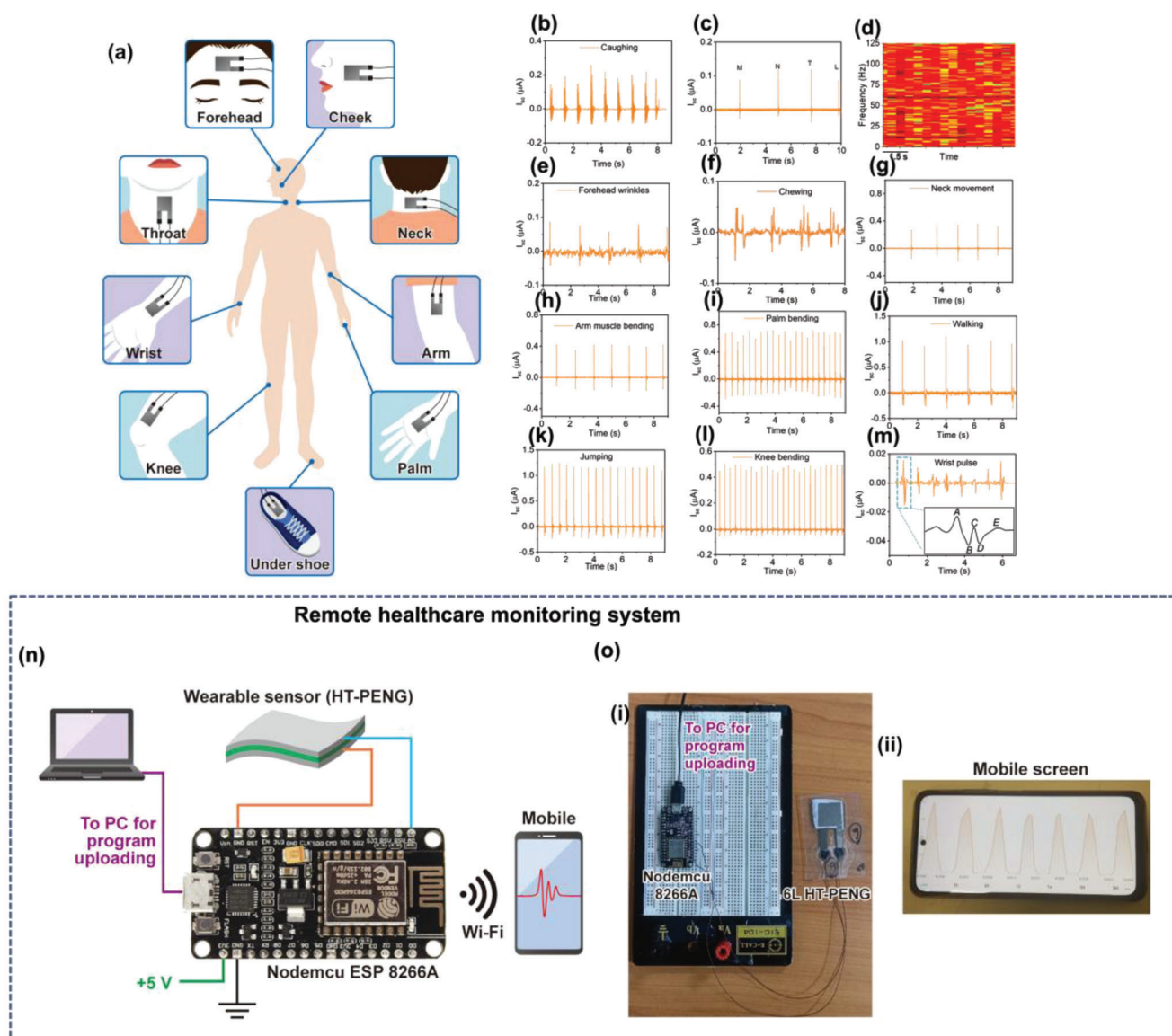


Figure 6. Real-time application of the HT-PENG as a self-powered wearable sensor in different parts of the human body for measuring biomedical activity. a) Human body showing the physiological signal monitoring locations. Output voltage generation from the 6L HT-PENG used to monitor different human activity: b) vocal cord vibrations: coughing action, c) vibrotactile output signals for different alphabets (M, N, T, and L) and its d) short-term Fourier transform (STFT) spectrogram, e) forehead wrinkling, f) chewing while eating, g) neck movement, h) arm muscle movement, i) palm bending, j) walking, k) jumping, l) knee joint motion, and m) wrist pulse, n) circuit diagram of the IoT based experimental setup. o) (i) Digital image of the practical circuit with (ii) mobile screen showing the received sensor data wirelessly using the Blynk app.

from tissue vibrations in the vocal cords during repeated coughing actions (Figure 6b). Furthermore, the proposed HT-PENG demonstrates its capacity to detect a speech recognition system. When pronouncing specific alphabets, such as M, N, T, and L, the device generated output signal patterns that mirrored the vocal cord vibrations (Figure 6c). The short-term Fourier transform (STFT) spectrograms of these signal patterns are displayed in Figure 6d. The STFT results reveal the frequency band spectrum of the spoken words within the 0–1000 Hz range, which falls within the standard range for vocal cord vibration frequency in healthy individuals.^[40] This finding suggests that the proposed HT-PENG has potential applications in the development of vi-

brotactile hearing aids designed to assist in speech rehabilitation training.^[64] It is essential to note that facial expressions of emotions, such as sadness, happiness, anger, confusion, and fear, possess a signal value indicative of an individual's current emotional state.^[65] In this context, variations in forehead wrinkles play a critical role in studying facial appearance and expressions in humans.^[66] In order to demonstrate this, the HT-PENG was attached to a person's forehead, and the corresponding sensor output is displayed in Figure 6e. The self-powered wearable sensor generated output signals that varied with forehead wrinkle changes, suggesting that the device may be utilized for studying patients' emotions or human emotional states, thereby

contributing to the development of human-machine interaction networks focusing on emotion. As a proof-of-concept for human motion detection activity, the HT-PENG was attached to various body parts, including the cheek, neck, arm, palm, knee, and wrist. Figure 6f illustrates the corresponding output voltages generated by cheek muscle movement during chewing. Figure 6g,h displays the output voltage responses to neck and arm muscle movements, respectively. These results indicate that the wearable device could potentially be employed for detecting or monitoring neck and arm muscle twitches and spasms that arise from involuntary muscle movements. Figure 6i shows the output voltage response corresponding to palm bending and releasing, primarily caused by epidermis deformation during palm closure and opening that impose tensile strain to the 6L HT-PENG.

The produced tensile strain by palm bending along the thickness direction of the HT-PENG (ϵ_y , parallel to the dipole orientation) was $\epsilon_y = \frac{L}{2r} = 0.35\%$, (where L (the thickness of the device) was $1140 \mu\text{m}$ and r (the bending radius) was 16 mm) and along the length direction of the device was $\epsilon_x = 0.11\%$ considering the Poisson's ratio, $\nu = |\frac{\epsilon_x}{\epsilon_y}| = 0.3$ of P(VDF-TrFE).^[67]

In addition, the HT-PENG was attached to a tester's shoe sole (preferably under the toe) using adhesive tape, and voltage output was measured during walking (Figure 6j) and jumping activities (Figure 6k). Due to the higher dynamic force from jumping the HT-PENG produced higher voltage than that of the walking activity.

Notably, no substantial performance loss was observed in the HT-PENG after multiple walking and jumping cycles. These results suggest that this device could be utilized in smart shoes for gait recognition and walking speed analysis while maintaining high stability under continuous stress. Furthermore, the wearable sensor was attached to the knee joint during the patellar reflex to monitor joint and leg muscle motion. Figure 6l displays the negative and positive pulses as the knee bends and releases. In addition to the harsh biomechanical energy harvesting, the HT-PENG can also detect subtle heart pulse signals in real-time by attaching the device to the wrist (Figure 6m). The detected heart rate was 80 beats per minute, with each peak denoting one pulse, which was close to the normal person at resting heart rate.^[68]

The morphological characteristic of the arterial pulse waveform is composed of four waves of systolic nature, that is, A-wave (initially positive), B-wave (early negative), C-wave (re-increasing), D-wave (late re-decreasing), and one wave of diastolic nature, that is, E-wave (positive) (inset of Figure 6m). In fact, the parameters used for monitoring cardiovascular dysfunctions such as, the ratio of peak heights such as E-, D-, and C-waves to A-wave (i.e., $P_{A/E} \approx 5.6$; $C/A \approx 0.24$; $D/A \approx -0.9$, respectively) and the time delay ($\tau_{EA} \approx 0.2$) between the A- and E-wave were consistent with the previously developed highly sensitive piezoelectric^[69] and triboelectric^[70] based healthcare monitoring sensors. This result indicates the prospective applicability of our developed sensor toward physiological signal monitoring sensor in near future. The superiority of the HT-PENG in biomechanical energy harvesting performance compared to previously reported PENGs is presented in Table S9 (Supporting Information). The summarized list of specific improvements of the 6L HT-PENG with respect to other PENGs described in the manuscript is presented in Table S10 (Supporting Information).

In addition to the wearable energy harvesting/sensing performance, the HT-PENG-based wireless remote health monitoring system was also demonstrated. The circuit diagram and schematic of the IoT-based remote health monitoring system is depicted in Figure 6n, featuring key components such as a single-chip ESP8266A Wi-Fi module and a PC/smartphone equipped with the Blynk app. The single-chip ESP8266A boasts a 512 KB Flash memory and a 10-bit analog-to-digital converter (ADC) set, running on a 32-bit microcontroller unit (MCU) with a Real-Time Operating System (RTOS). The digital-to-analog conversion (DAC) of the HT-PENG/sensor data value for processing is executed by the MCU. Once the waveforms have been processed, the corresponding data are transmitted to the local server, which is built using the ESP8266A HTTP protocol. The real-time practical circuit is illustrated in Figure 6o-i, showcasing the output response of the HT-PENG under gentle finger touch displayed on a smartphone screen (Figure 6o-ii) through the local server for the IoT-based remote healthcare monitoring system.

Medical professionals can swiftly review reports on this network via Wi-Fi using a smartphone or laptop. This remote health monitoring system has potential applications in developing smart point-of-care diagnostic devices that can alert healthcare staff in case of any abnormalities arise in the health status of patients without any direct contact with the person.

2.6. Self-Powered Water Level Sensing System

Additionally, we have demonstrated a battery-free water level sensing system that shows a promising application in smart home appliances (Figure S18, Supporting Information). This system can monitor the water level inside the tank/reservoir as shown in the display that also can help prevent water wastage during the filling process that aligns well with eco-friendly practices and environmental water conservation. The HT-PENG is connected to the full wave bridge rectifier followed by a capacitive filter to power up the commercial water level sensor as shown in the schematic (Figure S18a, Supporting Information). This system can measure the water level contained in the reservoir/tank. The real-time practical circuit of self-powered water level measuring system is illustrated in Figure S18b (Supporting Information) and the corresponding sensor signal output at different water level is displayed in Figure S18c (Supporting Information). To compare the performance of the commercial water level sensor with our HT-PENG, the water level sensor was also driven by a battery (Video S3, Supporting Information).

3. Conclusion

In summary, this study demonstrated a high-performance piezoelectric energy harvester with interspaced metal sheets based hetero-structured PENG (HT-PENG) by alternately stacking the BT NPs interfaced P(VDF-TrFE) and GNS embedded P(VDF-TrFE) electrospun nanofiber. In addition, a new strategy of Maxwell displacement current improvement in the composite nanofibers has been introduced in two ways: improving stress confinement/concentration effect and piezoelectric coefficient. The BT nanoparticles improved the piezoelectric coefficient of

the individual composite fibers up to 187.86 pC N^{-1} whereas GNS decreased the internal impedance of the composite fibers and consequently of overall devices that cumulatively enhanced the power output. The giant output voltage of 350 V, current of $6 \mu\text{A}$, and power output of 3.62 W m^{-2} easily drive the commercial electronic units demonstrating its potential applications toward self-powered portable electronics. In addition, the superior pressure sensitivity ($20 \pm 1.4 \text{ V kPa}^{-1}$) of the device was further used in several self-powered wearable sensing applications including but not limited to detecting different physiological signs from human body movement. Furthermore, a wireless healthcare system for remote health monitoring was also developed using the HT-PENG. In overall, giant energy harvesting performance, the superior pressure sensitivity, wide range pressure detection, stability, and ability to work under wireless condition makes the HT-PENG as a potential candidate to push the self-powered wearable devices toward commercialization in near future.

4. Experimental Section

Materials: Poly(vinylidene fluoride-co-trifluoroethylene) (P(VDF-TrFE)) (68/32) powder, Barium titanate (BaTiO_3) (BT) powder (diameter $\leq 100 \text{ nm}$), Graphite nanosheets (GNS) powder, Butan-2 one was obtained from Sigma-Aldrich Korea Co., Ltd., South Korea, and Ni-Cu coated polyester fabric electrodes were purchased from Solueta Co. Ltd, South Korea. All the chemicals were analytical reagent grade and used without any further purification.

Preparation of Pure P(VDF-TrFE) Nanofibers and Composite Nanofibers: First, the spinning solutions were prepared by dissolving 12 wt.% P(VDF-TrFE) in butan-2 one solvent, followed by stirring for 4 h at 60°C . Subsequently, GNS powder with different weight ratios (0.05, 0.10, 0.15, and 0.20 wt.%) was added into the above solution, which was then sonicated for 90 min at room temperature to ensure the homogeneous dispersion of GNS in the P(VDF-TrFE) matrix. Thereafter, the resulting solution was vigorously stirred for 8 h at 850 rpm at 60°C , and subsequently sonicated for 30 min at room temperature. The electrospinning solution was transferred into a 10 mL hypertonic syringe with a diameter of 0.8 mm to initiate the electrospinning process. The solution was dispensed through a syringe pump and injected into the needle at a flow rate of 1.2 mL h^{-1} . The nanofibers were deposited onto an aluminum foil wrapped over a rotating drum collector rotation speed of 80 rpm and tip-to collector distance of 10 cm was maintained.

The BT powder was incorporated into 12 wt.% P(VDF-TrFE) solutions at varying weight ratios (5, 10, 15, and 20 wt.%) in butan-2-one solvent to prepare BT-embedded P(VDF-TrFE) nanofibers. The fabrication process followed the method outlined in the previous section. A control solution containing 12 wt.% P(VDF-TrFE) without GNS or BT NPs was prepared and electrospun under identical conditions used to prepare the P(VDF-TrFE)/BT, and P(VDF-TrFE)/GNS composite nanofibers for comparative experiments. The pure P(VDF-TrFE) nanofibers were referred to as NPVF. All nanofibers based on P(VDF-TrFE)/GNS and P(VDF-TrFE)/BT and NPVF samples were dried at 60°C for 8 h to remove residual solvents and achieve stable nanofibers. The schematic illustration of the preparation of the electrospinning solution and experimental setup of the fabrication of electrospun nanofibers is shown in Figure S19 (Supporting Information). The thickness of the NPVF, optimized 0.10 wt.% GNS in P(VDF-TrFE) (referred as P0.10GNS), and 10 wt.% BT added P(VDF-TrFE) (referred as P10BT) composite nanofibers are shown in Figure S20 (Supporting Information). This study referred all P(VDF-TrFE)/BT nanocomposite nanofiber mats as P5BT, P10BT, P15BT, and P20BT as per 5–20 wt.% concentration of BT NPs. Similarly for P(VDF-TrFE)/GNS nanocomposite nanofiber mats as P0.05GNS, P0.10GNS, P0.15GNS, and P0.20GNS as per 0.05–0.20 wt.% concentration of GNS.

Fabrication of Single-Layered PENG (S-PENG): The schematic representation of the fabrication process for single-layered PENGs (S-PENG) based on varying weight percentages of BT NPs and GNS incorporated P(VDF-TrFE)/BT and P(VDF-TrFE)/GNS composite nanofibers is schematically illustrated in Figure S21i,ii (Supporting Information). Typically, the fabrication process involved cutting free-standing NPVF nanofibers, P(VDF-TrFE)/BT, and P(VDF-TrFE)/GNS composite nanofibers mats, utilized as the active layer, to the desired dimensions ($2.1 \text{ cm} \times 2.1 \text{ cm}$). These mats were then sandwiched between Cu–Ni polyester micro fabric electrodes, measuring $2 \text{ cm} \times 2 \text{ cm}$ to prevent electrical short circuits or charge leakage. Copper wires were connected to the top and bottom electrodes for external circuit integration. Finally, the entire assembly was encased in a PET adhesive tape to maintain the integrity of the composite nanofiber mats and shield them from external temperature fluctuations, and humidity. Optical image of the fabricated single-layered PENG is shown in Figure S21iii (Supporting Information).

Fabrication of Hetero-Layer PENG (HT-PENG): The detailed fabrication process of the hetero-layer PENG (HT-PENG) is schematically illustrated in Figure 1a. The HT-PENG was fabricated with an alternate layer arrangement of P10BT and P0.10GNS composite nanofibers. The Al metal foil was used as an interspace conductive electrode. For the systematic analysis of the HT-PENG, two layers (2layers), three layers (3layers), four layers (4layers), five layers (5layers), six layers (6 layers), and seven layers (7 layers) HT-PENG were fabricated. The cross-sectional scanning electron microscopy (SEM) image in Figure 1b, shows the overall device configuration with hetero-layer layer-by-layer configuration. The excellent flexibility of 6L HT-PENG and wearability of optimized composite nanofiber mats (10 wt.% BT added P(VDF-TrFE) and 0.10 wt.% GNS added P(VDF-TrFE) composite nanofibers mats) was demonstrated by wrapping them on a finger, as shown in Figure S22 (Supporting Information).

Characterizations: The surface morphology and elemental composition of the as-prepared electrospun NPVF, P(VDF-TrFE)/GNS, and P(VDF-TrFE)/BT composite nanofibers were investigated using Field emission scanning electron microscopy (FE-SEM) (JEOL, JSF7900F) at an acceleration voltage of 2.0 kV and EDS (Oxford instruments, Ultim Max) techniques. Before the SEM analysis, the as-prepared electrospun NPVF, P(VDF-TrFE)/GNS, and P(VDF-TrFE)/BT composite nanofibers were subjected to platinum sputtering at operational parameters of 90 s at a current of 0.1 mA. The vibrational bands and crystalline phases of the electrospun nanofibers were measured using FT-IR (PIKE Technologies, Spectrum 3 FT-IR). All the measurements were performed under attenuated total reflection (ATR) mode with the following measuring parameters: 4 cm^{-1} resolution and 20 scans. The XRD patterns of the electrospun nanofibers were obtained using an X-ray diffractometer (PANalytical, X'Pert Pro) with $\text{CuK}\alpha$ irradiation with a 2θ scanning range of 5° – 90° and a scanning speed of $8.5^\circ \text{ min}^{-1}$. The Laser Raman Spectroscopy was obtained using Laser Raman Spectrophotometer (Jasco, Model No. NRS-5100). Current (I)–Voltage (V) measurement was done by Keithley Source Meter (Model no. 2400). Lastly, the V_{oc} and I_{sc} responses from all the PENGs under different applied stress were recorded using a digital oscilloscope (Tektronix TDS 2014B) and low-noise current preamplifier (Stanford research systems, Model no. SR570), respectively. The high voltage probe (P5100A) had an input impedance of $40 \text{ M}\Omega \pm 1\%$. The applied hand imparting compressive force on the devices was estimated as previously reported works.^[71,72]

Supporting Information

Supporting Information is available from the Wiley Online Library or from the author.

Acknowledgements

This work was supported by the National Research Foundation of Korea (NRF) grant funded by the Korean government (MSIT) (no. RS-2022-00165505) and (no. 2020R1A5A8018367).

Conflict of Interest

The authors declare no conflict of interest.

Data Availability Statement

The data that support the findings of this study are available from the corresponding author upon reasonable request.

Keywords

barium titanate nanoparticles, graphite nanosheets, hetero-structured piezoelectric nanogenerators, nanocomposite nanofibers, stress concentration effects

Received: July 6, 2023

Revised: October 6, 2023

Published online: October 24, 2023

- [1] W. Deng, Y. Zhou, A. Libanori, G. Chen, W. Yang, J. Chen, *Chem. Soc. Rev.* **2022**, 51, 3380.
- [2] G.-T. Hwang, H. Park, J.-H. Lee, S. Oh, K.-I. Park, M. Byun, H. Park, G. Ahn, C. K. Jeong, K. No, H. Kwon, S.-G. Lee, B. Joung, K. J. Lee, *Adv. Mater.* **2014**, 26, 4880.
- [3] X. Cao, Y. Xiong, J. Sun, X. Zhu, Q. Sun, Z. L. Wang, *Adv. Funct. Mater.* **2021**, 31, 2102983.
- [4] H. Li, S. Lim, *J. Mater. Chem. A* **2022**, 10, 14894.
- [5] J. Zhu, S. Ji, J. Yu, H. Shao, H. Wen, H. Zhang, Z. Xia, Z. Zhang, C. Lee, *Nano Energy* **2022**, 103, 107766.
- [6] J. Zhu, Y. Zhu, X. Wang, *Adv. Mater. Interfaces* **2018**, 5, 1700750.
- [7] L. Persano, S. K. Ghosh, D. Pisignano, *Acc. Mater. Res.* **2022**, 3, 900.
- [8] Q. Xu, Z. Wang, J. Zhong, M. Yan, S. Zhao, J. Gong, K. Feng, J. Zhang, K. Zhou, J. Xie, H. Xie, D. Zhang, Y. Zhang, C. Bowen, *Adv. Funct. Mater.* **2023**, 33, 2304402.
- [9] L. Zhang, S. Li, Z. Zhu, G. Rui, B. Du, D. Chen, Y. F. Huang, L. Zhu, *Adv. Funct. Mater.* **2023**, 33, 2301302.
- [10] B. Mahanty, S. K. Ghosh, S. Jana, Z. Mallick, S. Sarkar, D. Mandal, *Sustainable Energy Fuels* **2021**, 5, 4389.
- [11] Y. Mao, P. Zhao, G. Mcconohy, H. Yang, Y. Tong, X. Wang, *Adv. Energy Mater.* **2014**, 4, 1301624.
- [12] J. Zhu, Y. Yang, H. Zhang, Z. Zhao, T. Hu, L. Liu, *Adv. Funct. Mater.* **2023**, 33, 2214859.
- [13] V. Sencadas, R. Gregorio, S. Lanceros-Méndez, *J. Macromol. Sci., Part B: Phys.* **2009**, 48, 514.
- [14] Y. Huang, G. Rui, Q. Li, E. Allahyarov, R. Li, M. Fukuto, G.-J. Zhong, J.-Z. Xu, Z.-M. Li, P. L. Taylor, L. Zhu, *Nat. Commun.* **2021**, 12, 675.
- [15] J. Kim, J. H. Lee, H. Ryu, J.-H. Lee, U. Khan, H. Kim, S. S. Kwak, S.-W. Kim, *Adv. Funct. Mater.* **2017**, 27, 1700702.
- [16] A. Gebrekrstos, T. S. Muzata, S. S. Ray, *ACS Appl. Nano Mater.* **2022**, 5, 7632.
- [17] S. Ramasundaram, S. Yoon, K. J. Kim, J. S. Lee, *Macromol. Chem. Phys.* **2008**, 209, 2516.
- [18] L. Persano, C. Dagdeviren, Y. Su, Y. Zhang, S. Girardo, D. Pisignano, Y. Huang, J. A. Rogers, *Nat. Commun.* **2013**, 4, 1633.
- [19] Y. Zhang, L. Zhou, X. Gao, C. Liu, H. Chen, H. Zheng, J. Gui, C. Sun, L. Yu, S. Guo, *Nano Energy* **2021**, 89, 106319.
- [20] L. Galhardo Pimenta Tienne, T. Brito De Abreu, F. Fabbri Gondim, B. De Salles Macena Da Cruz, G. Reis Martins, R. Antoun Simão, M. D. F. Vieira Marques, *Polym. Test.* **2020**, 91, 106790.
- [21] K. Maity, D. Mandal, *ACS Appl. Mater. Interfaces* **2018**, 10, 18257.
- [22] S. Siddiqui, H. B. Lee, D. Kim, L. T. Duy, A. Hanif, N.-E. Lee, *Adv. Energy Mater.* **2018**, 8, 1701520.
- [23] X. Du, Z. Zhou, Z. Zhang, L. Yao, Q. Zhang, H. Yang, *J. Adv. Ceram.* **2022**, 11, 331.
- [24] B. Sun, X. Li, R. Zhao, H. Ji, J. Qiu, N. Zhang, D. He, C. Wang, *J. Mater. Sci.* **2019**, 54, 2754.
- [25] C. R. Bowen, H. A. Kim, P. M. Weaver, S. Dunn, *Energy Environ. Sci.* **2014**, 7, 25.
- [26] H. Luo, X. Zhou, C. Ellingford, Y. Zhang, S. Chen, K. Zhou, D. Zhang, C. R. Bowen, C. Wan, *Chem. Soc. Rev.* **2019**, 48, 4424.
- [27] S. K. Ghosh, D. Mandal, *Nano Energy* **2018**, 53, 245.
- [28] J. Park, M. Kim, Y. Lee, H. S. Lee, H. Ko, *Sci. Adv.* **2015**, 1, e1500661.
- [29] W. Zeng, X.-M. Tao, S. Chen, S. Shang, H. L. W. Chan, S. H. Choy, *Energy Environ. Sci.* **2013**, 6, 2631.
- [30] Z. L. Wang, *Mater. Today* **2017**, 20, 74.
- [31] N. K. Das, M. Ravipati, S. Badhulika, *Adv. Funct. Mater.* **2023**, 2303288.
- [32] J. Shao, M. Willatzen, T. Jiang, W. Tang, X. Chen, J. Wang, Z. L. Wang, *Nano Energy* **2019**, 59, 380.
- [33] K. Dong, X. Peng, Z. L. Wang, *Adv. Mater.* **2020**, 32, 1902549.
- [34] Z. L. Wang, *Nano Energy* **2020**, 68, 104272.
- [35] Y. Park, Y.-E. Shin, J. Park, Y. Lee, M. P. Kim, Y.-R. Kim, S. Na, S. K. Ghosh, H. Ko, *ACS Nano* **2020**, 14, 7101.
- [36] W. K. Sakamoto, E. D. Souza, D. K. Das-Gupta, *Mater. Res.* **2001**, 4, 201.
- [37] H. Yu, T. Huang, M. Lu, M. Mao, Q. Zhang, H. Wang, *Nanotechnology* **2013**, 24, 405401.
- [38] C. Shuai, G. Liu, Y. Yang, F. Qi, S. Peng, W. Yang, C. He, G. Wang, G. Qian, *Nano Energy* **2020**, 74, 104825.
- [39] U. Yaqoob, A. S. M. I. Uddin, G.-S. Chung, *Appl. Surf. Sci.* **2017**, 405, 420.
- [40] V. A. Cao, M. Kim, S. Lee, C. G. Kim, P. C. Van, T. N. Thi, J.-R. Jeong, J. Nah, *ACS Appl. Mater. Interfaces* **2022**, 14, 26824.
- [41] Md M. Alam, S. K. Ghosh, A. Sultana, D. Mandal, *Nanotechnology* **2015**, 26, 165403.
- [42] K.-I. Park, M. Lee, Y. Liu, S. Moon, G.-T. Hwang, G. Zhu, J. E. Kim, S. O. Kim, D. K. Kim, Z. L. Wang, K. J. Lee, *Adv. Mater.* **2012**, 24, 2999.
- [43] J. Yan, M. Liu, Y. G. Jeong, W. Kang, L. Li, Y. Zhao, N. Deng, B. Cheng, G. Yang, *Nano Energy* **2019**, 566, 662.
- [44] J. Gomes, J. Serrado Nunes, V. Sencadas, S. Lanceros-Mendez, *Smart Mater. Struct.* **2010**, 19, 065010.
- [45] D. Mandal, S. Yoon, K. J. Kim, *Macromol. Rapid Commun.* **2011**, 32, 831.
- [46] B. Mahanty, S. K. Ghosh, S. Jana, K. Roy, S. Sarkar, D. Mandal, *Sustainable Energy Fuels* **2021**, 5, 1003.
- [47] X. Guan, B. Xu, J. Gong, *Nano Energy* **2020**, 70, 104516.
- [48] D. Ramesh, N. A. D'Souza, *Mater. Res. Express* **2018**, 5, 08530810.
- [49] Q. T. Ain, S. H. Haq, A. Alshammari, M. A. Al-Mutlaq, M. N. Anjum, *Beilstein J. Nanotechnol.* **2019**, 10, 901.
- [50] F. T. Johra, J.-W. Lee, W.-G. Jung, *J. Ind. Eng. Chem.* **2014**, 20, 2883.
- [51] S. K. Ghosh, J. Kim, M. P. Kim, S. Na, J. Cho, J. J. Kim, H. Ko, *ACS Nano* **2022**, 16, 11415.
- [52] R. P. S. Chakradhar, G. Prasad, P. Bera, C. Anandan, *Appl. Surf. Sci.* **2014**, 301, 208.
- [53] G. Ico, A. Showalter, W. Bosze, S. C. Gott, B. S. Kim, M. P. Rao, N. V. Myung, J. Nam, *J. Mater. Chem. A* **2016**, 4, 2293.
- [54] J. H. Jung, M. Lee, J.-I. Hong, Y. Ding, C.-Y. Chen, L.-J. Chou, Z. L. Wang, *ACS Nano* **2011**, 5, 10041.
- [55] S. K. Ghosh, D. Mandal, *Nano Energy* **2016**, 28, 356.
- [56] B. Mahanty, S. K. Ghosh, S. Garain, D. Mandal, *Mater. Chem. Phys.* **2017**, 186, 327.
- [57] M. K. Gupta, S.-W. Kim, B. Kumar, *ACS Appl. Mater. Interfaces* **2016**, 8, 1766.
- [58] B. Y. Lee, J. Zhang, C. Zueger, W.-J. Chung, S. Y. Yoo, E. Wang, J. Meyer, R. Ramesh, S.-W. Lee, *Nat. Nanotechnol.* **2012**, 7, 351.

- [59] D. Y. Park, D. J. Joe, D. H. Kim, H. Park, J. H. Han, C. K. Jeong, H. Park, J. G. Park, B. Joung, K. J. Lee, *Adv. Mater.* **2017**, 29, 1702308.
- [60] S. Xu, Y. Qin, C. Xu, Y. Wei, R. Yang, Z. L. Wang, *Nat. Nanotechnol.* **2010**, 5, 366.
- [61] J. Zou, M. Zhang, J. Huang, J. Bian, Y. Jie, M. Willander, X. Cao, N. Wang, Z. L. Wang, *Adv. Energy Mater.* **2018**, 8, 1702671.
- [62] B. Mahanty, S. K. Ghosh, K. Maity, K. Roy, S. Sarkar, D. Mandal, *Mater. Adv.* **2021**, 2, 4370.
- [63] K. Roy, S. Jana, S. K. Ghosh, B. Mahanty, Z. Mallick, S. Sarkar, C. Sinha, D. Mandal, *Langmuir* **2020**, 36, 11477.
- [64] N. Sebkhi, D. Desai, M. Islam, J. Lu, K. Wilson, M. Ghovanloo, *IEEE Trans. Biomed. Eng.* **2017**, 64, 2639.
- [65] S. Hareli, U. Hess, *Cogn. Emot.* **2012**, 26, 385.
- [66] S. Dayan, S. G. Yoelin, K. De Boulle, J. K. Garcia, *Aesthet. Surg. J. Open Forum.* **2019**, 1, ojz015.
- [67] S.-R. Kim, J.-H. Yoo, Y. S. Cho, J.-W. Park, *Mater. Res. Express* **2019**, 6, 086311.
- [68] S. Y. Kim, S. Jang, K. N. Kim, S. Lee, H. Chang, S. Yim, W. Song, S. Lee, J. Lim, S. Myung, *ACS Appl. Nano Mater* **2022**, 5, 15192.
- [69] S. K. Ghosh, J. Park, S. Na, M. P. Kim, H. Ko, *Adv. Sci.* **2021**, 8, 2005010.
- [70] S. K. Ghosh, J. Kim, M. P. Kim, S. Na, J. Cho, J. J. Kim, H. Ko, *ACS Nano* **2022**, 16, 11415.
- [71] S. K. Ghosh, A. Biswas, S. Sen, C. Das, K. Henkel, D. Schmeisser, D. Mandal, *Nano Energy* **2016**, 30, 621.
- [72] S. K. Ghosh, D. Mandal, *Appl. Phys. Lett.* **2016**, 109, 103701.